



# Interferometric Refractive Index Sensing with Terahertz Spoof Surface Plasmons

Y. Pan<sup>1,2</sup> · S. N. M. Hashim<sup>1</sup> · P. G. Huggard<sup>3</sup> · S. R. Andrews<sup>1</sup> 

Received: 19 February 2019 / Accepted: 2 April 2019 / Published online: 13 April 2019  
© The Author(s) 2019

## Abstract

Near field interference of spoof surface plasmons propagating on two opposing faces of a thin metal sheet waveguide perforated by a periodic array of tapered holes has been investigated by time-domain terahertz spectroscopy. Closely spaced, chirped spectral interference fringes are observed in the output near the field as a result of the different nonlinear dispersion of the two surface modes. Results illustrating the potential of such a structure for interferometric refractive index sensing of nanolitres of analytes are presented.

**Keywords** Metamaterials · Sensing · Terahertz · Refractive index · Interferometry

## 1 Introduction

The terahertz (THz) frequency spectrum is conventionally taken to be between about 0.1 and 10 THz and lies between microwaves which are the domain of electronics and the mid infrared, which is the domain of optics. Interest in this band is partly motivated by applications arising from the wealth of electronic and vibrational material excitations at THz frequencies and the quest for higher bandwidth signal processing and new imaging and sensing capabilities [1]. Examples include the dielectric characterisation of materials [2], dynamics of optically excited materials [3], medical diagnostics [4], pharmaceutical quality control [5], communications [6], security screening [7] and chemical and biochemical sensing [8]. Spectroscopic sensing applications frequently require the testing of small volumes of material. Waveguides or dielectric surfaces overlaid with metal films patterned with arrays of holes or resonators can be used to increase the sensitivity by confining the probing radiation to a sub-wavelength length scale in one or more dimensions. Various waveguide concepts that can be applied to sensing at

---

✉ S. R. Andrews  
s.r.andrews@bath.ac.uk

<sup>1</sup> Department of Physics, University of Bath, Bath BA2 7AY, UK

<sup>2</sup> Present address: Shenzhen Institute of Terahertz Technology and Innovation, Chentian Industrial Zone, Shenzhen, China

<sup>3</sup> RAL Space, STFC Rutherford Appleton Laboratory, Didcot OX11 0QX, UK

THz frequencies have been explored [9], including planar stripline resonators [10], parallel plate waveguides [11] and tightly bound surface waves on structured metal surfaces [12, 13].

Structured metal or metal-dielectric surfaces, often called metamaterial surfaces, can support tightly confined surface waves at terahertz frequencies with a dispersion relationship that mimics that of surface plasmon-polaritons in the visible but with a much lower effective plasma frequency that is determined by surface geometry rather than material choice [14]. The dispersion of these ‘spoof’ surface plasmon-polaritons (which we refer to as SSPPs hereafter) determines their spatial extent perpendicular to the surface. At terahertz frequencies, metals behave like near perfect electrical conductors and unstructured metal-dielectric interfaces cannot support tightly bound surface waves. Amongst the simplest metamaterial surfaces are flat metal films decorated with periodic arrays of blind or clear holes or grooves [12–16]. Here, the effective surface plasmon frequency is equal to the lowest cutoff frequency of the hole or groove cavity. In such structures, wavelength-scale out of plane confinement of surface waves is possible over roughly an octave of frequency [15]. By analogy with integrated optoelectronic architectures at optical frequencies, planar-like guiding structures at THz frequencies have advantages, in terms of possible integration with active components, for signal processing and sensing.

In this paper, we describe experiments and numerical simulations of an interferometric metamaterial sensor. It is based on SSPP propagation on opposing sides of an optically thick metal film pierced by a hexagonal close-packed array of tapered circular apertures with different effective diameters on the two faces. SSPPs on the two metamaterial surfaces are coupled via evanescent fields in the holes, analogous to the optical frequency surface plasmons on either side of metal films of a few tens of nanometre in thickness [17] but here, the coupling is relatively weak. The dispersion of symmetric and anti-symmetric THz SSPPs on an optically thin, 7- $\mu\text{m}$  thick, metal mesh in the simpler case that the two surfaces are equivalent has been studied previously by Ulrich and Tacke [18].

## 2 Materials and Methods

The mesh-like sample was made commercially using electroforming techniques [19] and is shown in Fig. 1a. It consists of a self-supporting 55- $\mu\text{m}$  thick nickel sheet perforated by a hexagonal close-packed array of tapered, approximately circular, apertures with a pitch  $g = 90 \pm 1 \mu\text{m}$ . The hole diameters on the top (t),  $z = +27.5 \mu\text{m}$ ,  $d_t = 77 \pm 1 \mu\text{m}$  and bottom (b),  $z = -27.5 \mu\text{m}$ ,  $d_b = 55 \pm 1 \mu\text{m}$  surfaces were determined from optical microscope images which also show that the surfaces are smooth on a few micrometre scale. Similar meshes have previously been studied as narrow band-pass filters in the far infrared [20]. They exhibit near unity normal incidence transmission at wavenumbers approximately equal to the inverse pitch and a rapid fall in transmission at a lower frequency which resembles that below cutoff in a waveguide and thus indicates thick rather than thin film behaviour.

Figure 1 b shows the experimental configuration used to study THz guiding along the  $x$ -direction (defined in Fig. 1a) in a 4 cm  $\times$  4 cm square of mesh cut with edges parallel to  $x$  and  $y$  and stretched flat over two metal bars leaving the top and bottom surfaces clear over a 3 cm width. Hyper-hemi-cylindrical silicon coupling lenses were placed 100  $\mu\text{m}$  from each end of the mesh. These end-fire coupling lenses relay the THz beam to fibre coupled photoconductive transmitters and receivers forming a time-domain spectroscopy system in which the receiver current varies with pump-probe delay in a similar manner to the transient THz electric field. A

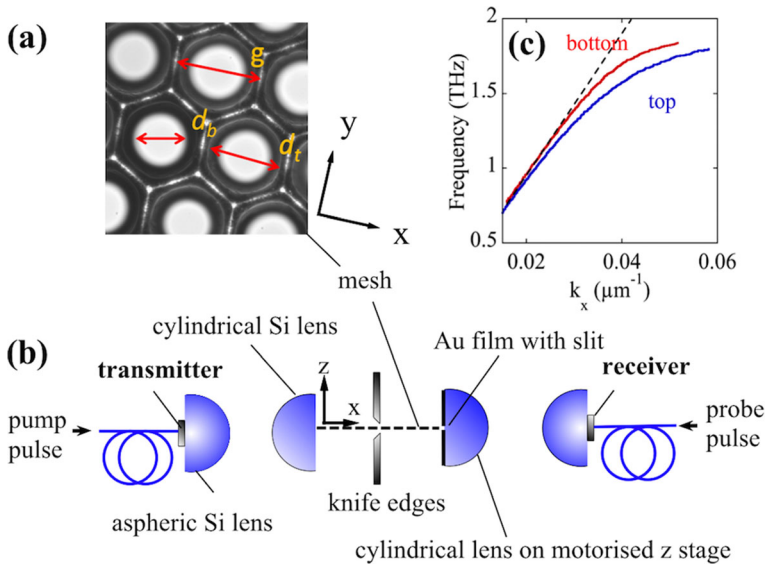


**Fig. 1** (Colour online) **a** Optical image of metal mesh structure. **b** Schematic of experimental fibre coupled setup. **c** Measured dispersion curves on upper and lower surfaces with the other surface covered by a metal plate. The dashed line shows the light line

similar arrangement has been described previously [21] but the present setup is modified a) by attaching the output-coupling lens to a motorised  $z$ -axis translation stage and b) by covering its flat input face with a 300-nm thick gold film which is continuous except for a 150- $\mu\text{m}$  wide central sampling aperture oriented along the  $y$ -axis, i.e. parallel to the mesh surface. This aperture in the detection system allowed crude ‘near field’ probing of the waveguide output field. A pair of steel razor blades was placed in the middle of the mesh with gaps of approximately 300  $\mu\text{m}$  between the blade edges and the top and bottom surfaces to minimise contributions to the signal from unguided radiation. The collimated THz beam incident on the input coupling lens had a 10-mm diameter (full width at half maximum amplitude) and the experiments were conducted in a dry air atmosphere.

To confirm the asymmetry between guiding on the top and bottom surfaces, a flat metal plate was attached to each of the surfaces in turn and the guided wave spectrum was measured. From the spectral phase data, the dispersion of SSPPs on the two surfaces for this blind hole case is obtained and shown in Fig. 1c. The top surface has larger effective diameter aperture and lower asymptotic cutoff frequency, so that over the frequency range investigated, the dispersion curve bends away from the light line more than for the bottom surface.

### 3 Results on Bare Mesh

Figure 2 a and b show typical time and frequency domain signals for three different  $z$  positions measured from the centre of the mesh, with the input beam approximately centred around  $z = 0$ . Interference from modes guided on the top and bottom surfaces of the mesh is clearly evident in the time domain for  $z = -103 \mu\text{m}$  and  $z = +87 \mu\text{m}$ : Fig. 2a. The corresponding spectra in Fig. 2b reveal a series of sharp dips, which move closer together with increasing frequency and are of different frequency above and below the centre of the film. The dips

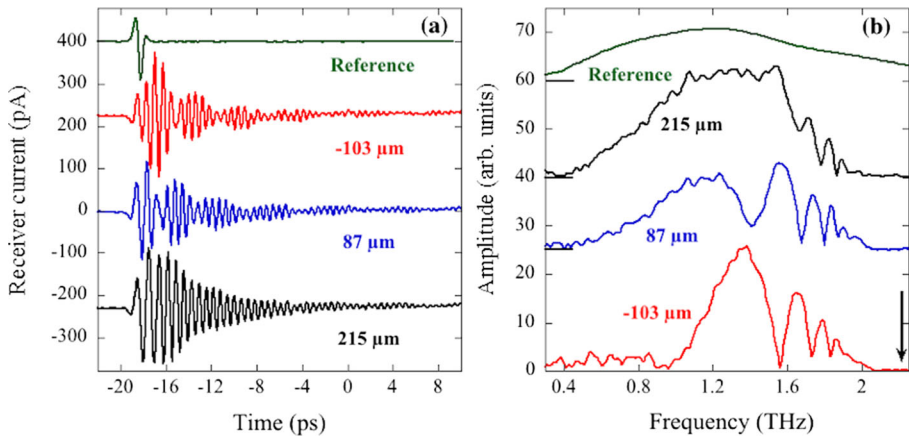


**Fig. 2** (Colour online) **a** Experimental time-domain traces measured  $100\ \mu\text{m}$  from the end ‘face’ of the mesh for different probe positions along  $z$  measured from the centre of the mesh compared with the free space reference signal obtained by removing the sample. **b** Spectra corresponding to the traces in (a): these have been displaced in amplitude for clarity. The arrow shows the zone boundary cutoff frequency

occur when the phase difference between radiation guided on the upper and lower surfaces is equal to an integer multiple of  $\pi$ . The observation of interference required placing the spatially resolving probe in the near field; interference was not evident in a far-field measurement. The chirped spectrum arises from the different nonlinear dispersion of SSPPs propagating on the top and bottom surfaces of the mesh. By moving to  $z = 215\ \mu\text{m}$ , we find a different spectrum with less pronounced dips because the radiation is predominantly collected from the top surface. If the modes have the same dispersion, then no spectral interference is expected, whilst modes with different linear dispersion would display equally spaced interference minima in the frequency domain. The asymptotic frequency of a SSPP mode is expected to be similar to the cutoff frequency of the dominant  $\text{TE}_{11}$  mode of a cylindrical waveguide, which for diameter  $d$ , has the value  $f_c = 0.586c/(dn)$  where  $n$  is the refractive index of the dielectric filling the cavity. Taking the largest mesh hole diameter, this formula gives a lower cutoff frequency of about 2.3 THz for air-filled holes, as indicated by the arrow in Fig. 2b. This is close to the zone boundary cutoff frequency for the propagation of the fundamental bound surface mode on either surface along the  $x$ -axis, which has the value  $2c/3g = 2.22\ \text{THz}$ . This suggests that interference might be observed up to a frequency similar to that of the zone boundary cut-off. Higher frequency surface modes undergo strong radiative damping and in any case lie outside the frequency range of the experiment.

Figure 3 compares measured, Fig. 3a, and simulated, Fig. 3b, spectra at probe positions above and below the plane of the mesh on logarithmic scales. The time-domain electromagnetic simulations were carried out using the finite integration technique [22] with a 3 THz bandwidth Gaussian input pulse. The mesh apertures were modelled as truncated cones with end diameters equal to those determined microscopically, periodic boundary conditions were imposed along  $y$  and the nickel mesh was given a conductivity of  $1.44 \times 10^7\ \text{S/m}$ . The input port was a  $300\text{-}\mu\text{m}$  high waveguide, centrally placed  $100\ \mu\text{m}$  from the mesh. The lowest order port mode was polarised perpendicular to the film. Virtual probes were positioned  $100\ \mu\text{m}$  from the output end at various  $z$  locations. Although the  $z$  positions in Fig. 3a and b are different, there is reasonable qualitative agreement, particularly in the occurrence of intensity maxima for  $z > 0$  at approximately the same frequencies as the intensity minima for  $z < 0$ . Quantitative agreement is not expected, mainly because the cross-

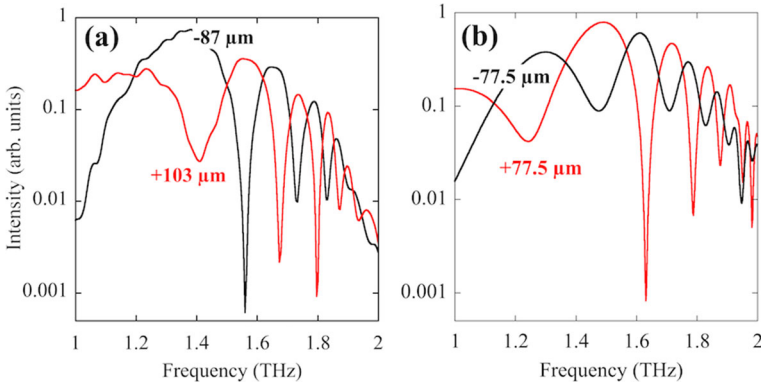


**Fig. 3** (Colour online) Comparison of experimental (a) and calculated (b) intensity spectra obtained for the indicated  $z$  probe positions above and below the centre of the mesh

sectional profile of the mesh apertures is more complicated than the assumed linear taper. There is a slight and shallow tapering from apertures on the upper surface and a more pronounced and deeper tapering from the bottom surface. The simulation also does not account for the focusing of the input beam and the limited spatial resolution of the experimental detection scheme.

It is notable that the effective Q-factors of the dips in Fig. 3a and b are as high as 50 and similar in magnitude to those reported for Fano resonances in transmission measurements on asymmetric split ring resonator arrays [23, 24] which have been suggested as potential platforms for refractive index sensing. In the asymmetric split ring case, high Q-factors are associated with low radiative damping. In the mesh case, high Q-factors are instead obtained by exploiting the narrow frequency interval between interference minima resulting from the shortened wavelength of tightly bound surface waves near cut-off.

A simple model of the spatial variation of the output spectrum can be constructed by assuming that the surface modes on each face are independent and have a dispersion relation of the form  $k_{t,b} = \frac{1}{c} \sqrt{\omega^2 + \alpha_{t,b} \omega^4 / (\omega_{t,b}^2 - \omega^2)}$  where the asymptotic SSPP frequencies are  $\omega_t$ ,  $\omega_b = 1.172\pi c/d_{t,b}$  and  $\alpha_{t,b} = 64(d_{t,b}/(\pi g))^4$  [14]. The coefficient  $\alpha_{t,b}$  is here defined for a square array of deep holes of side  $d_{t,b}$  and period  $g$  but the difference between square and hexagonal geometries is a small detail compared with the other approximations made. In particular, the wavelength-scale decay length of the SSPP into air is not explicitly treated but is instead crudely approximated by modelling the output end of the mesh as two line sources with a separation larger by 200  $\mu\text{m}$  than the mesh thickness. The choice of separation does not significantly affect the overall pattern. A calculated map of spectral amplitude as a function of spatial position and frequency for a mesh edge to probe plane separation of 200  $\mu\text{m}$  and frequency independent coupling to a 3 THz bandwidth Gaussian input pulse is shown in Fig. 4a. Although the model is grossly simplified, the chirped interference minima and the frequency shift of the peaks and dips in the spectrum above the mesh compared with those below are qualitatively reproduced. A more rigorous comparison with experiment was also performed using the finite integration technique described above and the resulting intensity-frequency map is shown in Fig. 4b. The frequency shift in the spectral interference pattern between the top and bottom surfaces seen in the experiment is again reproduced. In addition, wavelength-scale confinement of the surface waves and a fall in contrast of the spectral interference fringes for large  $|z|$  are revealed.

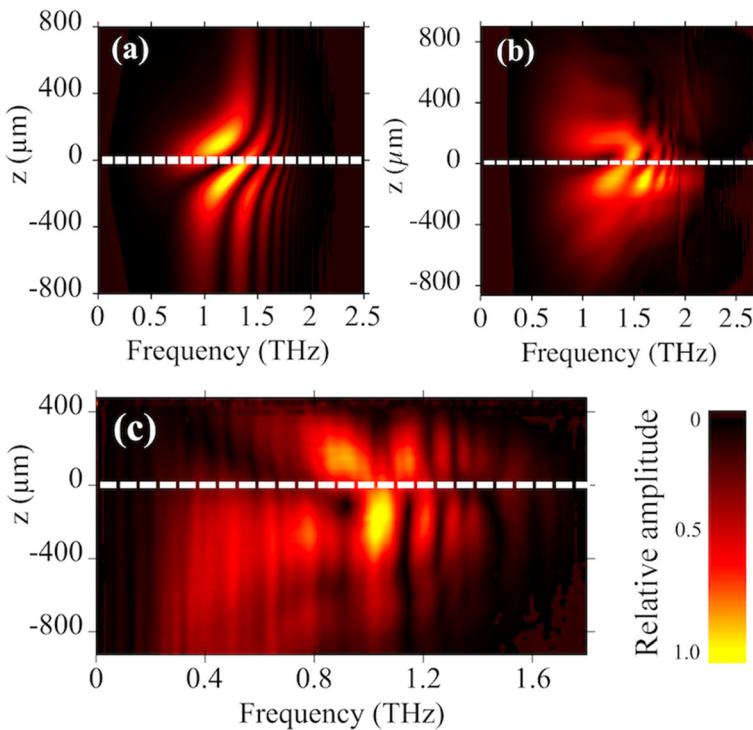


**Fig. 4** (Colour online) **a** Near field spectral amplitude maps for probe positions above and below the mesh ( $z=0$  position indicated by dashed line) in a plane positioned  $100\ \mu\text{m}$  from the output edge. Calculated for simple model dispersion curves on upper and lower surfaces. **b** Results of finite integration technique calculations. **c** Experimental spatial map for a wax filled mesh

#### 4 Refractive Index Sensing Using a Dielectric Filled Mesh

For sensing applications, planar surfaces on which analytes can easily be deposited and removed are desirable. Consequently, interference experiments were also performed on a sample of the mesh that was planarised by filling the apertures with wax. Adding the wax has the effect of reducing the asymptotic SSPP frequencies by a factor equal to the measured wax refractive index of 1.51 (near 1 THz), which yields better overlap of the frequency regime of prominent interference with that of high instrumental sensitivity. An intensity map showing the measured amplitude spectrum as a function of the detection aperture displacement for the wax-filled mesh is shown in Fig. 4c. Clear interference minima in the detected spectrum are again observed, particularly for  $z < 0$ . These are shifted downwards by an average of approximately 0.5 THz compared with the unfilled mesh. To test the sensing concept, the bottom surface of a  $20\ \text{mm} \times 20\ \text{mm}$  section of wax-filled mesh was spin coated with two different thicknesses of Shipley S1800 series photoresist [25] which has a measured refractive index close to 1.6 in the few THz range. The guided wave spectra were measured under nominally identical conditions, although there is a possible  $\pm 2\ \mu\text{m}$  repeatability error in the value of  $z$  when removing and replacing the mesh because of its low stiffness. The change in transmission spectrum measured at  $z = -150\ \mu\text{m}$  when 1.3- $\mu\text{m}$  and 2.4- $\mu\text{m}$  thick layers of resist are added can be seen in Fig. 5b. There is a clear frequency downshift in the spectral interference pattern with increasing resist thickness with a thickness sensitivity of approximately  $65 \pm 5\ \text{GHz}/\mu\text{m}$ . The shift is in reasonable agreement with

the response of approximately  $50 \text{ GHz}/\mu\text{m}$  estimated using the finite element simulations shown in Fig. 5b, and similar to results obtained in transmission experiments on planar metamaterials [23, 24]. The resist thickness of a few microns is much smaller than the wavelength-scale SSPP decay length into air so that this figure is not expected to change significantly with thickness for thicknesses below about  $100 \mu\text{m}$ . For comparison, the magnitude of the frequency shift per unit volume of added resist is roughly three times larger than that calculated for completely filling the holes in the mesh with resist.

## 5 Future Potential

The smallest volume of resist studied was about 400 nl. The planar waveguide geometry can in principle be improved to allow the study of smaller volumes by laterally confining the guided radiation for example by adiabatically tapering the width of the mesh along  $x$  so as to create a narrow waist where analytes can be deposited. Tests were carried out to establish whether such a structure would adequately support confined surface waves by laser-cutting a sample consisting of two  $30^\circ$  tapers bridged by a 4-mm long single row of holes in a bow-tie geometry. The far field-transmitted spectrum shows very little change in amplitude compared with the untapered case, which suggests that surface waves can be confined to a wavelength length scale in two dimensions with little radiative loss in this type of structure. A more versatile interferometer exploiting nonlinear SSPP dispersion on a single surface could be realised using deep silicon etching and conformal metal deposition techniques. A simple example is a pair of laterally graded blind hole or groove array guides [26] with different cutoff frequencies coupled to a source and detector using a pair of similarly constructed, tapered Y splitters. Such a device could feasibly be integrated with a microfluidic analyte deliver system. The application we envisage is the detection of small changes in the refractive index of a chemically or biologically active film in response to the addition of specific analytes that change the optical properties without significantly changing the thickness.

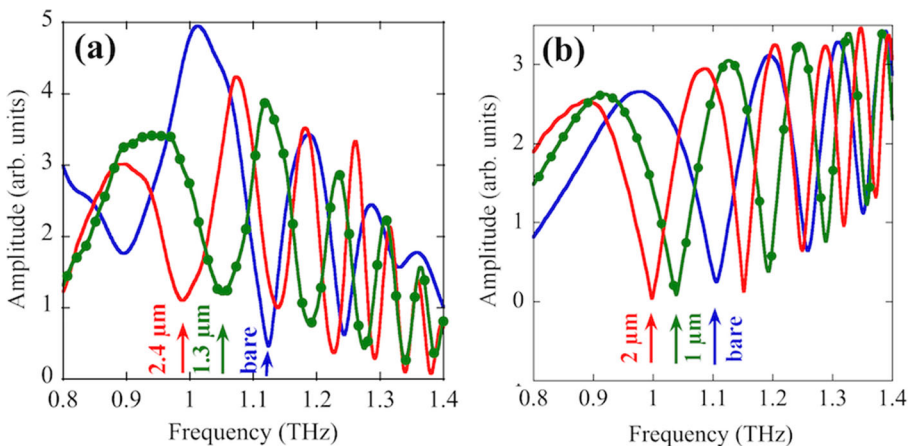


**Fig. 5** (Colour online) **a** Experimental spectra at  $z = -100 \mu\text{m}$  for a bare wax filled mesh and with the indicated thicknesses of photoresist deposited on the lower,  $z < 0$ , surface. **b** Calculated spectra for similar resist thicknesses. The curves with added symbols correspond in **a** to  $1.3 \mu\text{m}$  of resist and in **b** to  $1 \mu\text{m}$

## 6 Conclusions

In conclusion, we have demonstrated a terahertz interferometric sensing concept using a particularly simple metal mesh waveguide that exploits the nonlinear dispersion of spoof surface plasmon-polaritons. The sensitivity of the interferometer has the potential to be further improved using microfabrication techniques so as to allow detection of small changes in the refractive index of a chemically or biologically active film in response to the addition of small quantities of analytes.

**Funding Information** We thank the UK Engineering and Physical Science Research Council for part funding under grant EP/J007595/1. Y. Pan and S. N. M. Hashim thank the University of Bath and the Government of Malaysia respectively for financial support of studentships.

**Open Access** This article is distributed under the terms of the Creative Commons Attribution 4.0 International License (<http://creativecommons.org/licenses/by/4.0/>), which permits unrestricted use, distribution, and reproduction in any medium, provided you give appropriate credit to the original author(s) and the source, provide a link to the Creative Commons license, and indicate if changes were made.

## References

1. X.-C. Zhang and J. Xu, Introduction to THz wave photonics, New York, Springer (2010)
2. D. Grischkowsky, S. Keiding, M. van Exter and Ch. Fattinger, *JOSA B* **7**, 2006 (1990)
3. R. Ulbricht, E. Hendry, J. Shan, T. F. Heinz and M. Bonn, *Rev. Mod. Phys.* **83**, 543 (2011)
4. C. Yu, S. Fan, Y. Sun and E. Pickwell-MacPherson, *Quant. Imaging Med. Surg.* **2**, 33 (2012)
5. L. M. Ingle, A. M. Jaiswal, P. V. Vaidya, A. P. Kedar, *Int. J. of Pharmacy and Pharmaceutical Science Research* **3**, 48 (2013)
6. I. F. Akyildiza, J. Miquel Jornet and C. Hana, *Phys. Comm.*, **12**, 16 (2014)
7. E. Grossman, C. Dietlein, J. Ala-Laurinaho, M. Leivo, L. Gronberg, M. Gronholm, P. Lappalainen, A. Rautiainen, A. Tamminen, and A. Luukanen *Appl. Optics* **43**, 106E (2010)
8. M. Nagel, M. Forst and H. Kurz, *J. Phys. Conden. Matter* **18**, S601 (2006)
9. S. R. Andrews, *J. Phys. D: Appl. Phys.* **47**, 374004 (2014)
10. L. Dazhang, J. Cunningham, M. B. Byrne, S. Khanna, C. D. Wood, A. D. Burnett, S. M. Ershad, E. H. Linfield and A. G. Davies, *Appl. Phys. Lett.* **95**, 092903 (2009)
11. J. Q. Zhang and D. Grischkowsky, *Appl. Phys. Lett.* **86**, 061109 (2005).
12. B. You, J.-Y. Lu and J.-L. Peng, *Opt. Express* **21**, 21087 (2013)
13. B. Ng, S. M. Hanham, J. Wu, A. I. Fernandez-Dominguez, N. Klein, Y. F. Liew, M. B. H. Breese, M. Hong and S. A. Maier, *ACS Photonics*, **1**, 1059 (2014)
14. J. B. Pendry, L. Martin-Moreno, and F. J. Garcia-Vidal, *Science* **305**, 847–848 (2004).
15. C. R. Williams, S. R. Andrews, S. A. Maier, A. I. Fernandez-Dominguez, L. Martin-Moreno and F. J. Garcia-Vidal, *Nature Photonics* **2**, 175 (2008)
16. W. Zhu, A. Agrawal and A. Nahata, *Opt. Express* **16**, 6216 (2008)
17. J. Seidel, F. I. Baida, L. Bischoff, B. Guizal, S. Grafström, D. vanLabeke and L. M. Eng, *Phys. Rev. B* **69**, 121405(R) (2004)
18. R. Ulrich and M. Tacke, *Appl. Phys. Lett.* **22**, 251–253 (1973).
19. SPGPrints BV, 5830 AB Boxmeer, Holland.
20. P. G. Huggard, M. Meyringer, A. Schilz, K. Goller, and W. Prettl, *Applied Optics* **33**, 39–41 (1994).
21. C. R. Williams, M. Misra, S. R. Andrews, S. A. Maier, S. Carretero-Palacios, S. G. Rodrigo, F. J. Garcia-Vidal, and L. Martin-Moreno, *Appl. Phys. Lett.* **96**, 011101 (2010).
22. CST Studio Suite © © CST Computer Simulation Technology GmbH
23. R. Singh, W. Cao, I. Al-Naib, L. Cong, W. Withayachumnankul and W. Zhang, *Appl. Phys. Lett.* **105**, 171101 (2014)
24. I. Al-Naib, Y. Yang, M. M. Dignam, W. Zhang and R. Singh, *Appl. Phys. Lett.* **106**, 011102 (2015)
25. Microposit™ S1813® photoresist, Dow Electronic Materials
26. S. A. Maier and S. R. Andrews, *Appl. Phys. Lett.* **88**, 251120 (2006)

**Publisher's Note** Springer Nature remains neutral with regard to jurisdictional claims in published maps and institutional affiliations.